

REPORT

MOLECULAR DIFFUSION

Boosted molecular mobility during common chemical reactions

Huan Wang¹, Myeonggon Park^{1,2}, Ruoyu Dong¹, Junyoung Kim^{1,3}, Yoon-Kyoung Cho^{1,3}, Tsvi Tlusty^{1,2}, Steve Granick^{1,4*}

Mobility of reactants and nearby solvent is more rapid than Brownian diffusion during several common chemical reactions when the energy release rate exceeds a threshold. Screening a family of 15 organic chemical reactions, we demonstrate the largest boost for catalyzed bimolecular reactions, click chemistry, ring-opening metathesis polymerization, and Sonogashira coupling. Boosted diffusion is also observed but to lesser extent for the uncatalyzed Diels-Alder reaction, but not for substitution reactions S_N1 and S_N2 within instrumental resolution. Diffusion coefficient increases as measured by pulsed-field gradient nuclear magnetic resonance, whereas in microfluidics experiments, molecules in reaction gradients migrate “uphill” in the direction of lesser diffusivity. This microscopic consumption of energy by chemical reactions transduced into mechanical motion presents a form of active matter.

How to transduce chemical activity into motion is of mounting interdisciplinary interest in chemistry, biology, and physics (1–17). However, the known examples of how to do so on the molecular level were produced by nature to achieve biomolecular functions with molecular motors (2, 3) and catalytic enzymes (4–6) or in specially designed synthetic chemical systems (7–9), making their generality difficult to assess.

Our experiments show that common chemical reactions can produce mobility more rapid than Brownian diffusion. On the basis of the use of two independent techniques, pulsed field–gradient nuclear magnetic resonance (NMR) spectroscopy and gradient microfluidics, the findings cannot be attributed to gas production or convection and instead are qualitatively consistent with findings reported for catalytic enzymes (4–6, 15, 16), whose interpretation excites debate (17). Our interpretation of these findings suggests that a chemical reaction in liquids can be a nonlocal phenomenon with substantial mechanical perturbation of nearby solvent molecules over distances tens to hundreds of solvent molecules. This finding raises fundamental questions about how energy is funneled from reactants to products in the solvent environment.

To measure molecular diffusion in solution, we used pulsed field–gradient NMR spectroscopy, which provides chemical specificity regarding both the abundance and the mobility of multiple species in the same sample (18).

Experimental precautions that need to be taken against solution currents from convection are known (19, 20). Briefly, we labeled molecules spatially using a magnetic gradient along the NMR tube. Radio-frequency pulses with equal duration and opposite magnitude were applied as echo, with a set diffusion time (Δ) between them so that nondiffusing spins were unaffected but displacement of the diffusing ones was encoded as intensity attenuation (18). A time limitation of the latter is that the time for each scan must exceed the spin-lattice relaxation time (T_1) of nuclear spins, a number that can be hundreds of milliseconds for catalysts that contain a paramagnetic metal. Another limitation is that the method’s limited sensitivity demands numerous averaging scans to reach the needed signal-to-noise ratio.

Thus, we studied chemical reaction conditions with rates sufficiently slow to permit 3 to 5 min of signal averaging per data point and validity of the steady-state assumption that underlies the data analysis yet is sufficiently high to give adequate signal regarding mobility changes. Reactions were typically completed in ~2 hours. We confirmed the successful suppression of convection in a reaction known (20) to produce bulk convection (fig. S1) and used the same convection suppression pulses routinely (figs. S2 to S6). The successful suppression of convection artifacts lends confidence to the present measurements.

As summarized in table S1, we began by screening 15 organic reactions that could be run under mild conditions—for example, room temperature and standard pressure. The selected reactions spanned a wide range of thermodynamic driving force (reaction free energy) and reaction rate, and we considered both catalyzed and uncatalyzed reactions. Some

reactions with large thermodynamic driving force were, given the above-mentioned technical constraints, too rapid to follow, such as acid-base reactions, ketone-hydroxylamine condensations, and strain-promoted copper-free click reactions. Some were too slow to follow, such as unimolecular elimination. Some produce gas by-products, such as Grubbs ring-closing metathesis, tetrazine-strained alkene addition, and Staudinger ligation. From this screening, we identified four reactions—copper-catalyzed click, Grubbs ring-opening metathesis polymerization (ROMP), Sonogashira coupling, and Diels-Alder—during which molecular mobility was demonstrably more rapid than Brownian diffusion, whereas two other reactions (substitution reactions S_N1 and S_N2) showed null results. The parameters of the NMR experiments are listed in table S2. Although making comparisons between these different reactions in the same solvent would have been optimal, different solvents were needed to obtain the needed reaction rates.

In an example of a click reaction (21), the aqueous-phase copper (I) catalyzed 1,3-dipolar cycloaddition of an alkyne and an azide (Fig. 1A); a schematic depiction of the catalytic cycle is shown in Fig. 1B. Chemical shifts of different proton nuclei were monitored during the reaction, with raw data illustrated in fig. S2A, and from the peak heights as a function of time elapsed, we quantified the reaction kinetics. We monitored the solvent in which the catalyst was dispersed by using D_2O solvent containing H_2O tracer and found no dependence on tracer concentration in the range 0.4 to 2%. Raw data in pulsed-field gradients (figs. S3 and S4) gave the apparent translational diffusion coefficient D_{app} of different proton nuclei as a function of elapsed time, deduced from a log-linear plot of the signal intensity against b , a function of gradient field (G) squared, $I/I_0 = \exp(-D_{app}b)$, whose slope is D_{app} (figs. S5 and S6, and fits in tables S3 and S4). The high linearity we found experimentally (correlation coefficient > 0.9999) (Fig. 1C and table S3) validated the applicability of this method to analyze the data. Varying the diffusion time Δ by an order of magnitude, 10 to 100 ms, made no difference (fig. S7). We confirmed known Brownian diffusion coefficients—for example, $1.9 \times 10^{-9} \text{ m}^2 \text{ s}^{-1}$ before and after reaction for H_2O in D_2O from the chemical shift at 4.7 parts per million (ppm), and $1.0 \times 10^{-9} \text{ m}^2 \text{ s}^{-1}$ for ascorbate before reaction from chemical shifts at 4.8 and 3.7 ppm (for ascorbate, meaningful comparison was not possible after reaction given its complexation with copper ion). These control experiments lent credibility to the measurement of increased D_{app} during chemical reaction. In Fig. 1, D and E, we plot $\Delta D_{app}/D_0$, the relative diffusion increase over the Brownian diffusion coefficient of the same molecules.

¹Center for Soft and Living Matter, Institute for Basic Science (IBS), Ulsan 44919, South Korea. ²Department of Physics, Ulsan National Institute of Science and Technology (UNIST), Ulsan 44919, South Korea. ³Department of Biomedical Engineering, UNIST, Ulsan 44919, South Korea. ⁴Department of Chemistry, UNIST, Ulsan 44919, South Korea. *Corresponding author. Email: sgranick@gmail.com

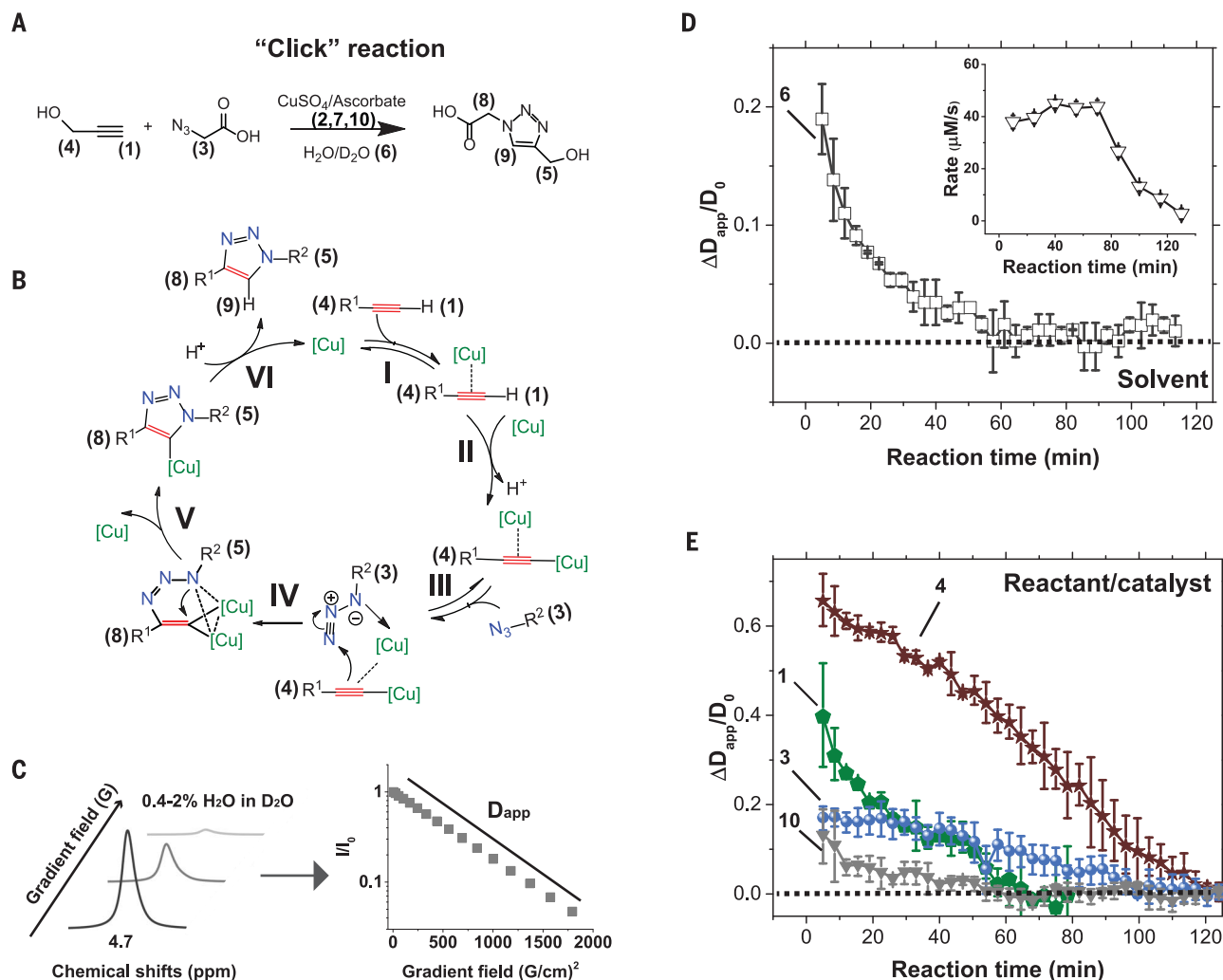


Fig. 1. Increased diffusion during click chemical reaction. (A) Reaction equation. The numbers correspond to the order of NMR shifts whose time dependence we track in (B) to (E) (fig. S2A). (B) Schematic depiction of the click reaction catalytic cycle, adapted from (29). Double arrows indicate reversible steps, and single arrows indicate irreversible steps. Intermediate reactions are identified by roman numerals. (C) Representative diffusion NMR

spectra showing that a magnetic gradient produces attenuation I/I_0 in magnetic gradient squared and linearity on the log-linear scale from which apparent diffusion coefficient is calculated. (D) Increased diffusion plotted against reaction time for solvent, with reaction rate plotted in the inset. (E) Increased diffusion plotted against reaction time for the reactant and catalyst. Reaction conditions: 0.25 M reactant, 20 mM catalyst, in 0.4 to 2% H_2O -doped D_2O .

The earliest time point measurements were ~5 min after mixing the reactants, the time to mount the NMR tube and align it. The diffusion of water increased similarly as much (Fig. 1D and fig. S2A, peak 6) as for the catalyst Cu-ascorbate complex, which had a molar mass an order of magnitude greater, 240 g mol^{-1} (Fig. 1E, gray curve, and fig. S2A, peak 10). During subsequent reaction, the diffusion increase lessened but more slowly than would be consistent with a single exponential process. Comparing with reaction rate, which is the rate of reactant consumption (Fig. 1D, inset), the diffusion rate increased, whereas chemical reaction rate remained constant. In other experiments, we changed the reactant concentration. For higher reactant concentrations, increased diffusion persisted longer (fig. S8),

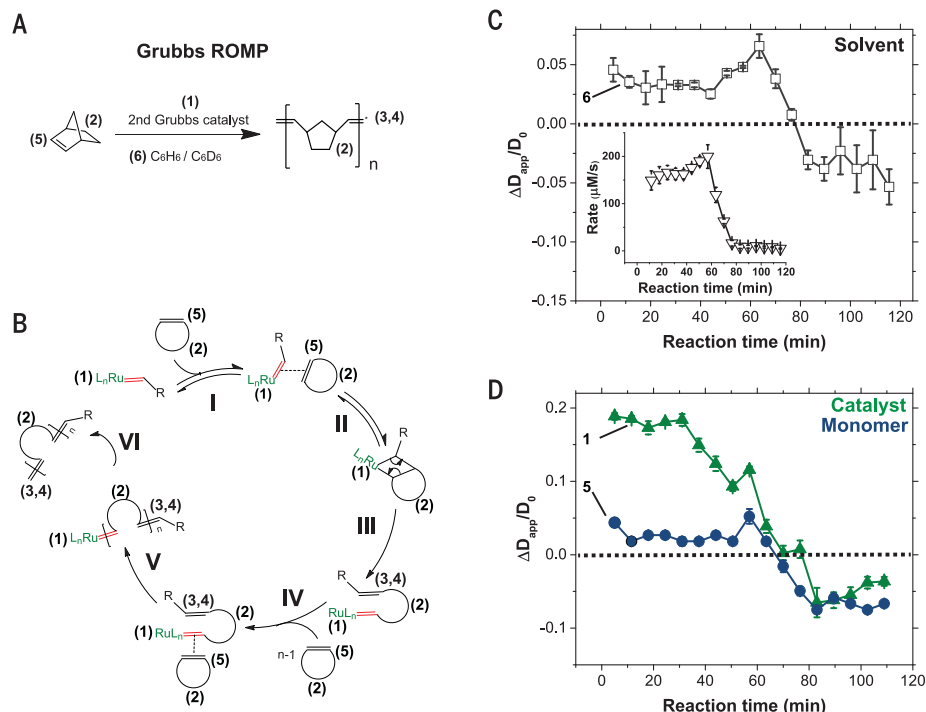
but the maximum amount of increase was unaffected. Below, we discuss the possible dependence on catalyst concentration.

The click reaction is exothermic, but exothermicity alone did not explain the observed increase of up to 20%. First, temperature rise was $<1.5^\circ\text{C}$ (fig. S9), which is too small by an order of magnitude because diffusion coefficient is usually proportional to absolute temperature and inversely proportional to viscosity. Physical considerations show that local temperature pulses dissipated too rapidly to be relevant (5). Pulses of heat from local reaction events might produce convection on nanometer and micrometer scales. We conducted simulations of heat transfer (supplementary text) and did not find support for this hypothesis (fig. S10).

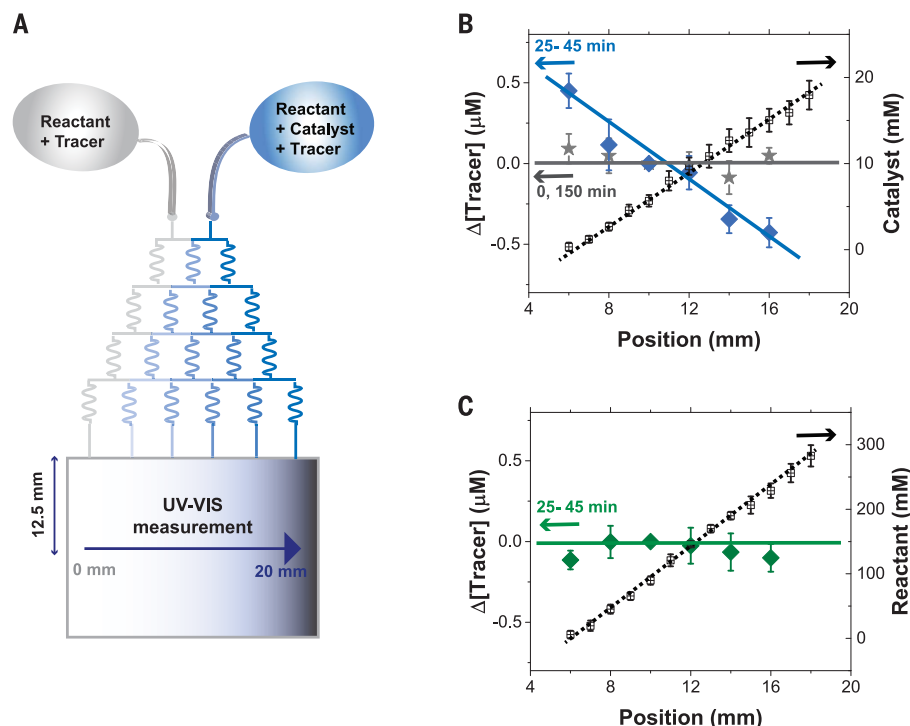
Olefin metathesis through the ruthenium-catalyzed (Grubbs catalyst) ROMP of norbornene to polynorbornene (Fig. 2, A and B) (22) showed similar patterns. The solvent was benzene, a nonpolar molecule, so its consistency with findings for the aqueous click reaction showed that the effects we report were neither solvent nor metal-catalyst specific. Diffusion of both solvent (Fig. 2C) and catalyst (Fig. 2D) increased while the reaction took place, and we tracked the reaction kinetics (Fig. 2C, inset). We monitored the catalyst diffusion coefficient from the ligand chemical shift (figs. S2B, S11, and S12 and fits in table S5) and observed an initial increase of ~15%, followed by decay, which was consistently higher than solvent diffusion increase throughout the reaction time. These trends correspond to the Grubbs catalyst

Fig. 2. Increased diffusion during Grubbs-catalyzed ROMP.

(A) Reaction equation. The numbers correspond to the order of NMR shifts whose time dependence we track in (B) to (D) (fig. S2B). (B) Schematic depiction of the catalytic cycle, adapted from (22). Double arrows indicate reversible steps, and single arrows indicate irreversible steps. Intermediate reactions are identified by roman numerals. (C) Increased diffusion plotted against reaction time for solvent with reaction rate plotted in the inset. (D) Increased diffusion plotted against reaction time for the monomer and catalyst. Reaction conditions are 1 M reactant, 0.12 mM catalyst, in 2 to 10% C₆H₆-doped C₆D₆.

**Fig. 3. Increased diffusion induces antichemotaxis.**

(A) Microfluidic gradient chip and inverse relation of reaction gradient and tracer gradient for click reaction. Condition is the same as in Fig. 1. Reaction gradient is produced by the catalyst gradient across the chip as mixture containing catalyst is infused from one sole inlet, with the same tracer concentration in both inlets. Tracer molecules close to catalysts are most strongly influenced by the momentum of local hydrodynamic flow. (B) Reaction produces dynamic tracer concentration profile across the channel, determined with spatially resolved UV-vis absorption measurement. Change of tracer concentration (left ordinate) and catalyst concentration (right ordinate) are plotted against position normal to flow during reaction (25 to 45 min) and after reaction is completed (150 min). (C) Control experiment testing for antichemotaxis in a large reactant concentration gradient gives a null result in the absence of catalyst.



requiring an initiation time (Fig. 2B, intermediate steps I, II, and III) before reaching maximum catalytic efficiency. Because the catalyst attaches to the end of propagating polymer chain (Fig. 2B, intermediate steps IV and V) during ROMP, the mass of the diffusing molecule should increase by the 92 g mol⁻¹ per catalysis cycle (23). We confirmed that the increase of viscosity in the system created by the

growing polymer chains slowed diffusion of reactant molecules (Fig. 2D). Thus, by the end of reaction, the catalyst diffusivity was ~5% slower than before reaction started, unlike the click reaction, which after completion had produced no permanent diffusivity changes and hence, by inference, no viscosity change.

Sonogashira coupling is a more complex system because it uses cocatalysts. This reaction

forms a carbon-carbon bond between terminal alkyne and aryl halide through a main palladium catalyst and a copper cocatalyst (figs. S13 to S15 and fits in table S6). Our fourth to sixth examples were noncatalyzed reactions, Diels-Alder (figs. S16 to S18 and fits in table S7), S_N2 (figs. S19 to S21 and fits in table S8) and S_N1 (figs. S22 to S24 and fits in table S9). The results for the S_N1 and S_N2 reactions gave

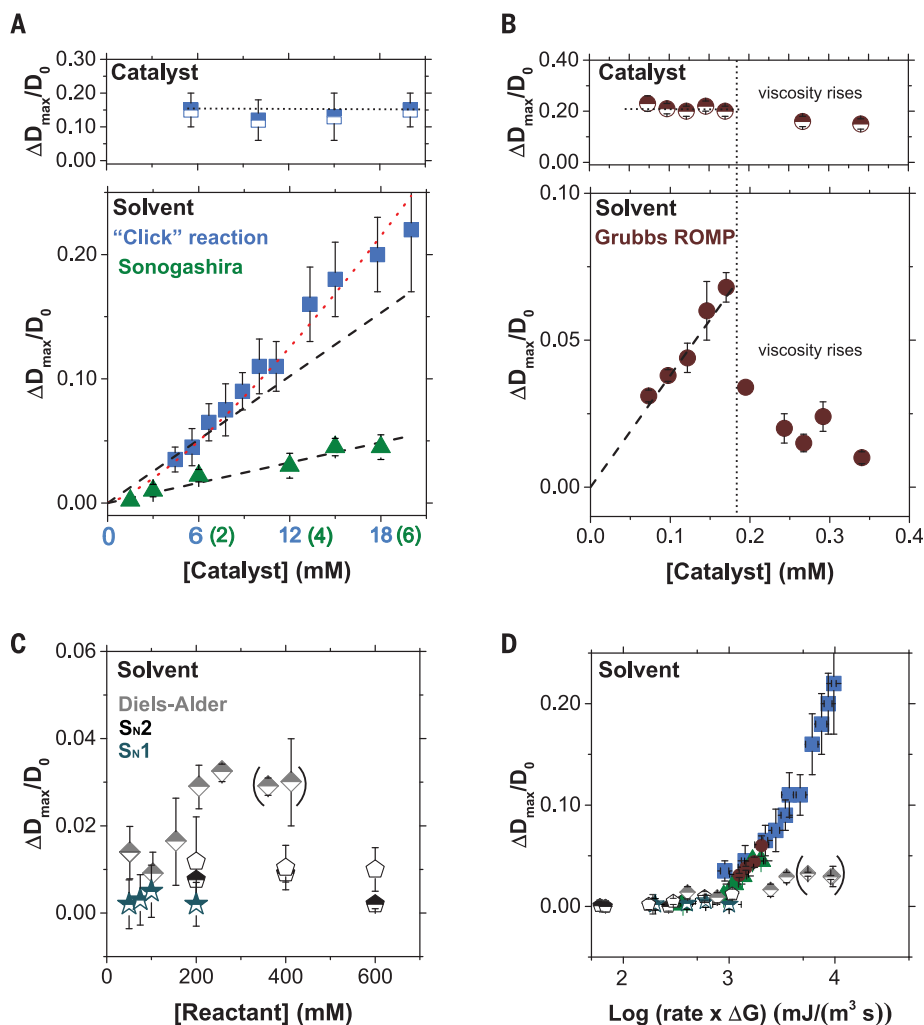


Fig. 4. Summary of five chemical systems. (A to D) Click, Grubbs ROMP, Sonogashira reaction, and noncatalyzed reactions: Diels-Alder (rhomboids), S_N1 (stars), S_N2 at (open pentagons) and above (half-filled pentagons) room temperature as specified in the supplementary materials. Ordinates are maximal normalized increased diffusion plotted against catalyst concentration regarding [(A) and (B)] catalyst diffusion and [(A), (B), and (C)] solvent diffusion. Lines with slope 1 (black dashed) and power 4/3 (red dotted) are guides to the eye. (D) Maximal normalized increased diffusion is plotted against free-energy release rate by using the thermodynamic parameters in table S10. Points in parentheses are believed less reliable because the rate of this second-order reaction is highest in the beginning, so its maximum was likely missed in these measurements averaged over 10 to 15 min per datum.

putative findings of up to 1% diffusion increase, which we consider to be a null result given the experimental uncertainty. The Diels-Alder addition of maleimide and furfurylamine showed 1 to 3% diffusion increases, which was greater than the experimental uncertainty.

Our last example used an independent experimental method. Microfluidics-based experiments allowed us to set up catalyst gradients to test the prediction that when chemical stimuli form a gradient, migration of catalyst, reactant, and nearby solvent up (or down) this gradient should display spatially dependent D_{app} values of the kind observed long ago for the different problem of bacteria chemotaxis

(24) and more recently for catalytic enzymes (6). To implement this approach to follow solvent diffusion, we added a dye of high absorbance to water for the click reaction and measured its spatially resolved ultraviolet-visible (UV-vis) absorbance to gauge local water diffusivity, near the channel middle to avoid possible wall boundary effects downstream from the channel entry (12.5 mm downstream with laminar flow of $100 \mu\text{m s}^{-1}$). This stratagem was needed because for technical reasons, it was not feasible to directly spatially resolve molecules that participated in the chemical reactions. Fluorescence detection, which could be more sensitive, suffers

from quenching from the azide reagent of click chemistry.

A glass microfluidic chip adapted from earlier studies (6, 16) was used to produce uniform reactant and dye concentrations accompanied by linear gradients of catalyst concentration across the width of the microfluidic channel (Fig. 3A). Plotting change in local dye concentration (left ordinate) and local catalyst concentration (right ordinate) against position across width of the channel (Fig. 3B), we observed that the initially uniform dye concentration (0 min) adopted a concentration gradient with slope opposite to that of the catalyst gradient (25 to 45 min). After the reaction ended, the dye concentration reverted to homogeneity (150 min).

Ruling out origin from the reactant gradient alone, we performed a control experiment without catalyst but with a large gradient of reactant concentration and observed a null result (Fig. 3C), which was as expected because the gradient produces negligible concentration difference across the nanometer size of these molecules. The conceptual issue—how it is possible on physical grounds to have a stable, spatially dependent concentration gradient—was sorted out in the context of bacteria chemotaxis (24, 25). Applying those ideas to this situation, conserving constant fluid density in the face of increased diffusion of molecules in the vicinity of catalysis events requires a counterbalanced backflow of mostly solvent molecules. As the concentration gradients stabilized toward steady state, the net currents of catalyst and solvent, including the backflow, vanish (24, 25). We interpret these findings to confirm those from diffusion NMR.

What governs magnitude? The concentration dependence in all of these systems is summarized in Fig. 4, A to C. We surveyed and summarized relevant thermodynamic properties, noting that values computed from density functional theory (DFT) can have a large scatter. The free energy change ΔG , enthalpy change ΔH , activation energy barrier, activation volume ΔV , maximum reaction rate, and boosted diffusion for all of the reactions reported are summarized in table S10. Taken together, the data for catalyzed reactions over a range of catalyst and reactant concentrations, 0.1 to 20 mM for catalysts and 50 mM to 1 M for reactants, fall empirically on a master curve so that the mobility increase depends on the energy release rate, the product of ΔG times rate (Fig. 4D), with increase observed only beyond a threshold. As $\Delta G \approx \Delta H$, the data correlate similarly with ΔH . The results for the S_N1 and S_N2 reactions are below the threshold, likely suggesting that null results for these reactions (within experimental uncertainty) signifies that threshold energy release rate was not reached. For intramolecular alkyne cyclization, from the maximum energy

release rate one can anticipate increased diffusion of 2 to 3% according to this correlation, which is within the standard deviation of data reported in an earlier study (20, 26) and consistent with the null result reported (20).

At energy release rates beyond the threshold, a diffusion increase was observed for Diels-Alder cycloaddition, but the magnitude was less than for the catalyzed reactions. This difference may indicate the prominent contribution of kinetic intermediates because catalytic reactions have broad time scales, broader than single-step reactions, and also multiple elemental reactions during each catalytic cycle. It is likely that multiple factors—including activation energy barrier, rate-limiting step, kinetic reversibility of individual elemental steps, and characteristic time scales of intermediates (supplementary text)—could all contribute to the magnitude of diffusion increase.

That catalyst diffusion is unaffected by catalyst concentration (Fig. 4, A and B) signifies that this is a single-particle property. At the same time, overall solvent mobility scales much more strongly with catalyst concentration (Fig. 4, A to C). Millimolar catalyst concentrations boosted the overall solvent mobility by 2 to 20%. We interpret this to signify that moving reaction centers coupled to nearby solvent hydrodynamically (1, 11, 12, 14). As for the concentration dependence, data over limited concentration spans were consistent with the linearity drawn as guide to the eye (Fig. 4, A and B), complicated in the case of ROMP by viscosity rise. For the click reaction (Fig. 4A), it was possible to achieve the most extended concentration range, giving data more consistent with the power 4/3. Viewing the catalysts as units of “active matter” (10–14), they are predicted to induce velocity disturbance that decays as the inverse distance squared $v \sim 1/r^2$, boosting the diffusion by a factor that increases as 4/3 power of catalyst concentration, $\Delta D_{\max}/D_0 \sim v^2 \sim 1/r^4 \sim c^{4/3}$, as evidenced by the click reaction. For the cases of more limited concentration spans, linear and 4/3 power laws are practically indistinguishable (supplementary text and fig. S25). Taken together, from all of these data, boosted solvent diffusion appears to a nonlocal phenomenon, with the reacting centers producing substantial mechanical perturbation of surrounding solvent.

The largest activation energy step often correlates to the rate-determining step in a chemical reaction, so transition states likely account for some of the differences we report. For example, catalysis speeds up reaction by lowering the activation barrier. Specifically, activation volume is larger for 1,3 dipolar addition ($\sim -65 \text{ \AA}^3/\text{molecule}$) (27) and Diels-Alder (~ -65 to $-50 \text{ \AA}^3/\text{molecule}$) reactions than for substitution reactions ($< -30 \text{ \AA}^3/\text{molecule}$) (28). Unfortunately, values have not to our knowledge been reported for click (copper-catalyzed 1,3 dipolar addition), Grubbs-ROMP, or Sonogashira reactions, which possess multiple, incompletely elucidated transition states during their catalytic cycles, with the extra complication of precatalysis initiation.

Full understanding of these effects is likely to require consideration of not only barrier crossing rates but also ramifications of electronic structure changes during chemical reaction. These rapid electronic changes, manifested as electric field changes, will require solvated solvent molecules to reorganize—a long-range readjustment process in the environment that is slower than actual changes of the electronic structure. On physical grounds, we conjecture the likely mechanism to be that this mode of energy release produces transient translational motion of reacting centers at the nanoscale, accompanied by their random reorientations to produce a random walk over distances of tens to hundreds of solvent molecule dimensions. Conformational changes likely contribute (5, 15) but cannot fully explain the results because the common S_N2 reaction (figs. S19 to S21) produced null results despite the Walden conformation inversions that they are known to experience during reactions over the same regime of reaction rate as for the click reaction. Our findings suggest a breakdown of the classical chemistry paradigm that chemical reactions and diffusivity are uncoupled. The empirical correlations presented to summarize the magnitude of boosted diffusion, although imperfect, may be useful to estimate the effect in as-yet untested reactions.

REFERENCES AND NOTES

1. K. Kanazawa, T. G. Sano, A. Cairoli, A. Baule, *Nature* **579**, 364–367 (2020).
2. R. D. Vale, R. A. Milligan, *Science* **288**, 88–95 (2000).
3. M. J. Shelley, *Annu. Rev. Fluid Mech.* **48**, 487–506 (2016).

4. S. Sengupta et al., *J. Am. Chem. Soc.* **135**, 1406–1414 (2013).
5. R. Golestanian, *Phys. Rev. Lett.* **115**, 108102 (2015).
6. A.-Y. Jee, S. Dutta, Y.-K. Cho, T. Tlusty, S. Granick, *Proc. Natl. Acad. Sci. U.S.A.* **115**, 14–18 (2018).
7. J. Li, B. Esteban-Fernández de Ávila, W. Gao, L. Zhang, J. Wang, *Sci. Robot.* **2**, eaam6431 (2017).
8. V. García-López et al., *Nature* **548**, 567–572 (2017).
9. A. Coskun, M. Banaszak, R. D. Astumian, J. F. Stoddart, B. A. Grzybowski, *Chem. Soc. Rev.* **41**, 19–30 (2012).
10. B. Liebchen, H. Löwen, *Acc. Chem. Res.* **51**, 2982–2990 (2018).
11. S. Ramaswamy, *J. Stat. Mech. Theory Exp.* **2017**, 054002 (2017).
12. R. Kapral, A. S. Mikhailov, *Physica D* **318–319**, 100–104 (2016).
13. C. Bechinger et al., *Rev. Mod. Phys.* **88**, 045006 (2016).
14. M. C. Marchetti et al., *Rev. Mod. Phys.* **85**, 1143–1189 (2013).
15. J. Agudo-Canalejo, P. Illien, R. Golestanian, *Nano Lett.* **18**, 2711–2717 (2018).
16. A.-Y. Jee, Y.-K. Cho, S. Granick, T. Tlusty, *Proc. Natl. Acad. Sci. U.S.A.* **115**, E10812–E10821 (2018).
17. M. Feng, M. K. Gilson, *Annu. Rev. Biophys.* **49**, 87–105 (2020).
18. E. O. Stejskal, J. E. Tanner, *J. Chem. Phys.* **42**, 288–292 (1965).
19. I. Swan et al., *J. Magn. Reson.* **252**, 120–129 (2015).
20. T. S. C. MacDonald, W. S. Price, R. D. Astumian, J. E. Beves, *Angew. Chem. Int. Ed.* **131**, 19040–19043 (2019).
21. H. C. Kolb, M. G. Finn, K. B. Sharpless, *Angew. Chem. Int. Ed.* **40**, 2004–2021 (2001).
22. O. M. Ogba, N. C. Warner, D. J. O’Leary, R. H. Grubbs, *Chem. Soc. Rev.* **47**, 4510–4544 (2018).
23. M. Yasin, P. Liu, I. K. Tennie, A. F. M. Kilbinger, *Nat. Chem.* **11**, 488–494 (2019).
24. M. J. Schnitzer, S. M. Block, H. C. Berg, E. M. Purcell, *Symp. Soc. Gen. Microbiol.* **46**, 15–34 (1990).
25. P. F. Tupper, X. Yang, *Math. Phys.* **468**, 3864–3881 (2012).
26. T. S. C. MacDonald, W. S. Price, J. E. Beves, *ChemPhysChem* **20**, 926–930 (2019).
27. B.-B. Ni et al., *Chem. Commun.* **49**, 10130–10132 (2013).
28. T. Asano, W. J. Le Noble, *Chem. Rev.* **78**, 407–489 (1978).
29. B. T. Worrell, J. A. Malik, V. V. Fokin, *Science* **340**, 457–460 (2013).

ACKNOWLEDGMENTS

We thank D. Frenkel, B. Grzybowski, and K. Schweizer for discussions. **Funding:** This work was supported by the taxpayers of South Korea through the Institute for Basic Science, project code IBS-R020-D1. **Author contributions:** H.W. and S.G. conceived and designed the project and wrote the paper. H.W. did experiments. M.P. contributed to experiments. R.D. analyzed heat effects. J.K. and Y.-K.C. designed the microfluidic chip. T.T. did physical analysis. All coauthors reviewed and approved the final manuscript. **Competing interests:** The authors declare no competing interests. **Data and materials availability:** All data are available in the main text or the supplementary materials.

SUPPLEMENTARY MATERIALS

science.sciencemag.org/content/369/6503/537/suppl/DC1
Materials and Methods
Figs. S1 to S25
Tables S1 to S10
References (30–53)

9 January 2020; accepted 2 June 2020
10.1126/science.aba8425